Back-propagating rupture evolution within a curved slab during the 2019 Mw 8.0 Peru intraslab earthquake

Yaping Hu*[,a], Yuji Yagi[b], Ryo Okuwaki[b, c, d], Kousuke Shimizu[a]

[a] *Graduate School of Life and Environmental Sciences, University of Tsukuba, Ibaraki 305-8572, Japan*

[b] *Faculty of Life and Environmental Sciences, University of Tsukuba, Ibaraki 305-8572, Japan*

[c] *Mountain Science Center, University of Tsukuba, Ibaraki 305-8572, Japan*

[d] *COMET, School of Earth and Environment, University of Leeds, Leeds LS2 9JT, UK*

Summary

The 26 May 2019 M_W 8.0 Peru intraslab earthquake ruptured the subducting Nazca plate where the dip angle of the slab increases sharply and the strike angle rotates clockwise from the epicentre to north. To obtain a detailed seismic source model of the 2019 Peru earthquake, including not only the rupture evolution but also the spatiotemporal distribution of focal mechanisms, we performed comprehensive seismic waveform analyses using both a newly developed flexible finite-fault teleseismic waveform inversion method and a back-projection method. The source model revealed a complex rupture process involving a back-propagating rupture. The initial rupture propagated downdip from the hypocentre, then unilaterally northward along the strike

* Corresponding Author
yaping-hu@geol.tsukuba.ac.jp (Yaping Hu)

of the slab. Following a large slip occurring ~50–100 km north of the hypocentre, the rupture propagated bilaterally both further northward and back southward. The spatial distribution of focal mechanisms shows that the direction of T-axis azimuth gradually rotated clockwise from the epicentre northward, corresponding to the clockwise rotation of the strike of the subducting Nazca plate, and the large-slip area corresponds to the high-curvature area of the slab iso-depth lines. Our results show that the complex rupture process, including the focal-mechanism transition, of the Peru earthquake was related to the slab geometry of the subducting Nazca plate.

Keywords: Waveform inversion, Body waves, Earthquake dynamics, Earthquake source observations, Dynamics: seismotectonics, Dynamics and mechanics of faulting, Subduction zone processes

1. Introduction

Intermediate-depth (70–300 km) earthquakes (Gutenberg and Richter, 1949) occurred within the subducting slab that located beneath or near inland may cause particularly serious damages (e.g. McCloskey et al., 2010; Melgar et al., 2018; Ye et al., 2020). The generation mechanisms of these intraslab earthquakes are still hot-debated. The dehydration embrittlement of the subducting slab due to the high temperature environment in the mantle (e.g. Hacker et al., 2003; Houston, 2007; Di Toro et al., 2011; Derode and Campos, 2019), periodic viscous shear heating instabilities (e.g. Kelemen & Hirth, 2007; Prieto et al., 2013) or adiabatic shear instability (e.g. Renshaw and Schulson, 2013) have been considered as cause of intermediate-depth earthquakes. One of the obstacles to understanding the intermediate-depth earthquakes (especially depth deeper than 100 km) is low activity of aftershocks (e.g. Persh and Houston 2004a). Since it is difficult to estimate the fault size and geometry from aftershock activity, the source characteristics have been estimated mainly by analysing the complex broadband waveforms (e.g. Persh and Houston, 2004b; Tocheport et al., 2007). The moment (M_0) and duration (τ) scaling relation for the deep and intermediate-depth earthquakes has been systematically investigated using the broadband P-waveforms, which shows $\tau \propto M_0^{0.25\sim0.26}$ (Persh and Houston, 2004b; Poli and Prieto, 2014). According to the results of the dynamic and kinematic finite-fault analysis, the rupture process of large intermediate-depth earthquakes is influenced by the complex stress distribution (e.g. Ide and Takeo, 1996) and the heterogeneities of subducting slab (e.g. Twardzik and Ji, 2015) .

On 26 May 2019, a great normal-fault earthquake struck Peru and adjacent areas. The U.S. Geological Survey (USGS) determined the origin time 07:41:15 (UTC) on 26 May 2019, the hypocentre on 122.6 km deep at 5.812°S, 75.270°W, and the moment magnitude (M_W) 8.0. The 2019 Peru earthquake is the largest event ever recorded in northern Peru (Wong et al., 2012; Villegas-Lanza et al., 2016), one of the most seismically active zones in the world (Perfettini et al, 2010; Sladen et al., 2010), where the oceanic Nazca plate is subducting beneath the South America plate (Somoza and Ghidella, 2005; Prezzi and Silbergleit, 2015) (Fig. 1). The 2019 Peru earthquake is the largest intermediate-depth earthquakes listed in the Global Centroid Moment Tensor (GCMT) Catalog in the last 45 years (Dziewonski et al., 1981; Ekström et al. 2012). The distribution of hypocentral depths of intermediate-depth (70–300 km) earthquakes near the source region is consistent with slab depth changes. According to the GCMT catalog (Dziewonski et al., 1981; Ekström et al., 2012), the focal mechanism of most intraslab earthquakes is normal faulting (Fig. 1). Before the 2019 Peru earthquake, intense seismicity was observed in slab-bending zones, such as between 1.0°S and 2.5°S, and between 7.5°S and 9.5°S, but no large earthquake had been recorded in the source area of the 2019 event. Previous studies applied the conventional finite fault inversion to tele-seismic broadband waveforms found that the rupture propagated northward along steeply east-dipping nodal plane in a narrow rupture zone (Ye et al., 2020; Liu and Yao, 2020).

In this study, we applied the flexible finite-fault inversion method developed by Shimizu et al. (2020) to the teleseismic body waves of the 2019 Peru earthquake, and then estimated the T-axis azimuth distribution of the obtained focal mechanism distribution to evaluate the relationship between T-axis azimuth variation and the stress field related to the slab geometry.

One problem in interpreting the source model of an intermediate-depth earthquake is that it is generally difficult to select a primary fault plane from the two possible nodal planes obtained by moment tensor inversion (e.g., the GCMT solution). Because of the low aftershock activity of most intermediate-depth earthquakes, including the 2019 Peru earthquake (Ye et al., 2020), the aftershock distribution may not directly indicate the primary fault plane. In this study, the primary fault plane of the 2019 Peru earthquake was evaluated by the integrated use of waveform inversion and back-projection (BP). BP is useful for tracking the spatiotemporal source evolution of specific seismic phases during large earthquakes (e.g., Ishii et al., 2005; Krüger and Ohrnberger, 2005), but the depth resolution of the method is generally low (Yagi et al., 2012; Kiser and Ishii, 2017). In contrast, finite-fault inversion using teleseismic body waves have better resolution in depth (e.g., Yagi et al., 2004). Complementary use of BP and finite-fault inversion thus helps us to estimate both the rupture evolution and the primary fault plane. Finally, we compared the distributions of the high-frequency radiation sources and the slip rate distribution on the primary fault plane and then constructed an integrated source model from which we inferred the detailed rupture process of the 2019 Peru earthquake.

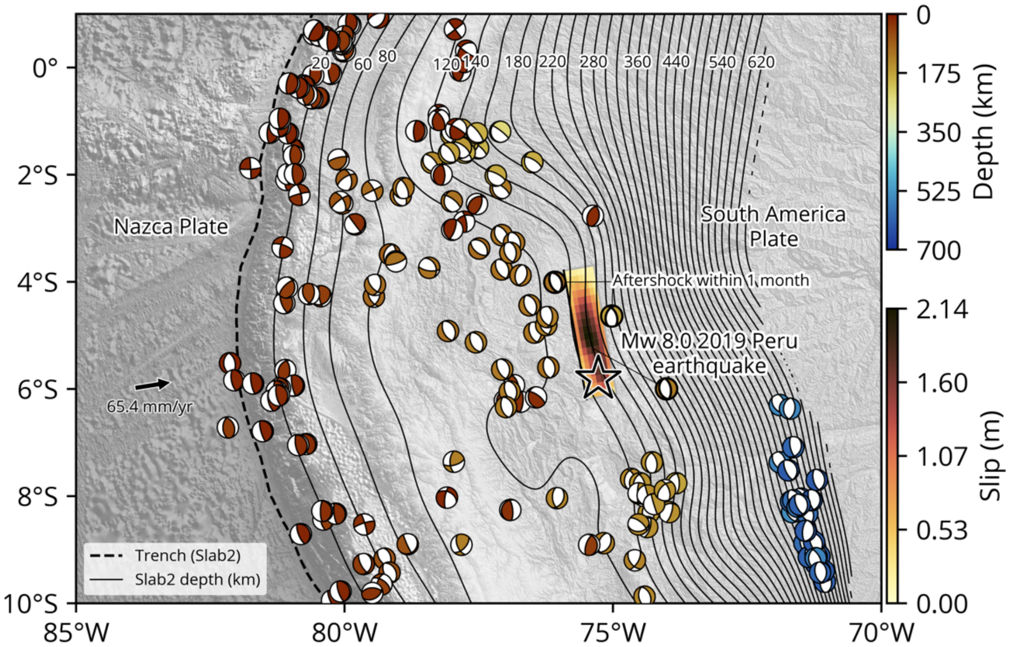

Figure 1: Overview of the source region of the 2019 Peru earthquake. Black and dashed lines indicate depth contours of Slab2 model (Hayes et al., 2018) at an interval of 20 km and trench, respectively. The beach balls show the GCMT solutions (Dziewonski et al., 1981; Ekström et al. 2012) of the Mw > 5.5 earthquakes occurred in 1976–2019. The colour of beach balls represents depth. The thick black-outlined beach balls are the aftershocks of the Peru earthquake within one month. Black arrow shows the relative motion of the Nazca plate (DeMets et al., 2010). The slip distribution on the map if from our preferred model (N1) for the 2019 Peru earthquake. The star shows the epicentre. The rectangle outlines the model plane geometry, and the black line is a top of the model plane.

2. Data and methods

We used the vertical components of teleseismic *P*-wave data from the Data Management Center of the Incorporated Research Institutions for Seismology (IRIS-DMC) recorded by stations within an epicentral distance between 30° and 90°. Teleseismic *P* waveforms recorded at 41 stations (Table S1) with adequate quality and good azimuthal coverage were selected for use in both the finite-fault inversion and BP (Fig. 2). We chose the teleseismic *P* waveform because of its well-defined data covariance components in the inversion formulation (Yagi and Fukahata, 2011) and its clear first-motion rise, which can be reliably picked. The first motion of the *P*-phase was manually picked, and the data were converted to velocity data. Then, the velocity waveforms were resampled at 0.8 s intervals for the finite-fault inversion.

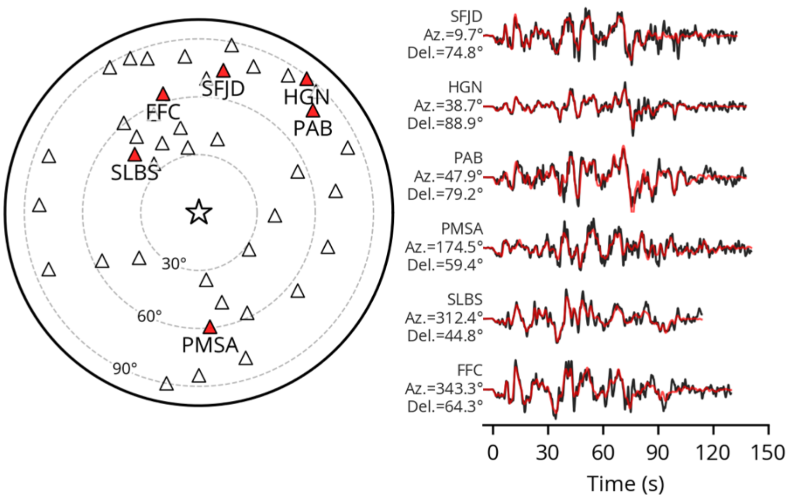

Figure 2: Distribution of teleseismic stations (triangles) and selected waveform fitting between observed (black) and synthetic waveforms (red). The synthetic waveforms are from the results using the N1 fault plane. The star denotes the epicentre. The station code, azimuth and epicentral distance are shown on the left of each panel.

Finite-fault inversion has been widely used since the 1980s for estimating the spatiotemporal slip-rate distribution of earthquakes (e.g., Olson and Apsel, 1982; Hartzell and Heaton, 1983). A linear finite-fault inversion can be used to obtain the slip-rate distribution on an assumed model plane. However, because we never know the true velocity structure under the surface and can rarely get the detailed information of fault geometry, the uncertainty of the Green's function and the uncertainty of the fault geometry together make it difficult to estimate seismic source models in a stable manner (e.g., Yagi and Fukahata, 2011; Duputel et al., 2014; Ragon et al., 2018; Shimizu et al., 2020). Recently, Shimizu et al. (2020) proposed a flexible finite-fault inversion method that mitigates the effect due to the uncertainty of the fault geometry by obtaining the distribution of seismic potency tensors (i.e., spatiotemporal distribution of slip and the fault geometry) along the assumed model plane, and that also mitigates the effect of the uncertainty of the Green's function by appropriately setting the data covariance matrix following Yagi and Fukahata (2011) (see Text S2 and Fig. S6). In the flexible finite-fault inversion method, fault slip along the assumed model plane is represented by the superposition of five basis double-couple components (Kikuchi and Kanamori, 1991); then, the possible fault geometry can be inferred from the spatiotemporal variation of focal mechanisms. Thus, to reveal both the slip-rate evolution and fault geometry of the 2019 Peru earthquake, we applied flexible finite-fault inversion to teleseismic *P* waves.

In this study, we set a model plane and assumed that fault slip occurred in the vicinity of this model plane (called the "fault plane" hereafter). Because it is difficult to select the primary fault plane from the two nodal planes of a moment tensor solution, we tested two different fault plane geometries (called N1 and N2) based on the USGS W-phase moment tensor solution (N1: strike = 350°, dip = 53°; N2: strike = 166°, dip =

37°) (https://earthquake.usgs.gov/earthquakes/eventpage/us60003sc0/moment-tensor, last accessed on 2021-06-15). For both the N1 and N2 models, we considered the fault plane to be 270 km long and 105 km wide, with along-strike 18 grid and along-dip 7 grid cells spaced at 15 km intervals in both the strike and dip directions. The theoretical Green's function with a sampling rate of 0.1 s was calculated by the method of Kikuchi and Kanamori (1991). We adopted the hypocentre determined by the USGS as the initial rupture point. For the velocity structure model near the source, we used a one-dimensional velocity model modified from the inferred velocity structure in the Peru region (Kaila et al., 1999; Ma and Clayton, 2014) (Table 1). The travel time, ray parameters, and geometrical spreading factors were calculated based on the ak135 reference velocity model (Kennett et al., 1995). For the slip-rate function at each source node, we adopted a linear B-spline function with a temporal interval of 0.8 s and a maximum duration of 55 s, and we assumed the slip rate to be zero after 80 s. We tested maximum rupture-front velocities from 2.5 to 5.0 km/s (Fig. S1). In the range of 2.5 to 3.5 km/s, the major rupture area expanded as the assumed maximum rupture-front velocity increased, but in the range of 4.0 to 5.0 km/s (Fig. S1), this dependency became indistinct. In addition, fluctuations of the moment rate function (Fig. S1) were similar among the tested rupture-front velocities. The first peak was during 0–15 s (the initial rupture), and the largest peak was during 15–80 s (the main rupture). On the basis of these results, we selected 4.0 km/s as the maximum optimum rupture-front velocity.

Table 1. Velocity model used for calculating Green's function

V_P (km/s)	V_S (km/s)	Density (10^3 kg/m^3)	Thickness (km)
6.00	3.47	2.70	20
6.66	3.85	2.90	20
7.10	4.13	3.05	30
7.80	4.50	3.25	30
8.10	4.70	3.38	90
8.60	5.00	3.55	0*

*0-km thickness means the semi-infinite velocity layer below the moho depth.

BP is a method used to obtain the spatio-temporal distribution of seismic radiation sources by waveform stacking that can provide information on rupture acceleration and deceleration (e.g., Uchide et al., 2013; Okuwaki et al., 2015). The interference between *P* and the depth phases (e.g., *pP* waves) when staking waveforms is known to degrade the BP images especially for the large shallow earthquakes (Yagi et al., 2012; Fukahata et al., 2014). However, as shown in the synthetic test of the BP method (Fig. S5), the effect of the interference of the depth phases is not significant, and the later events (>30 s) are well resolved. This is because the 2019 Peru earthquake was an intermediate-depth earthquake, and the *P* phase and the later depth phases were well separated, making it possible to acquire less-biased BP images (e.g., Suzuki and Yagi, 2011) from which to reliably estimate rupture velocity and, therefore, infer the detailed rupture evolution. Thus, the combined interpretation of the slip models and back-projection images allows the causative fault plane to be deduced – not one method alone either by the finite-fault model or the BP image. In our study, we used the BP method to obtain the primary fault plane and to infer the detailed rupture process, including rupture acceleration and deceleration. To enable comparison of the BP results with the finite-fault inversion, we used the same velocity waveform dataset for the BP as for the waveform inversion (Figs. 2 and S2). Butterworth band-pass filters of 0.3 to 2.0 Hz and 0.1 to 0.5 Hz were applied to the velocity waveforms, and then the data were resampled at 0.05 s intervals. We adopted nonlinear *n*th root stacking ($n = 3$) (Muirhead and Datt, 1976) to improve the signal-to-noise ratio of the BP images. The BP images are projected on the 320 km long and 200 km wide fault planes with the same strike and dip angles of the N1 and N2 fault planes, and the spatial grid interval of the possible source area was set to 2 km, which is fine enough to resolve high-frequency radiation sources. The BP procedure adopted in this study is evaluated by the synthetic test (Fig. S5), and we confirm that the input sources are robustly resolved.

3. Results

We constructed two seismic source models, one for each of the two fault plane geometries, N1 and N2 (Fig. 3). In both the N1 and N2 models, the rupture is concentrated in the area from 30 km south to 200 km north of the hypocentre in the along-strike direction. The dominant northern rupture propagation is found on both the two fault planes which is commonly observed in the previous studies (Ye et al., 2020; Vallée et al., 2020; Liu and Yao, 2020); while the rupture propagates eastward on the N1 fault plane and westward on the N2 fault plane.

The focal mechanisms in the large-slip area indicate normal faulting, but a small strike-slip component was obtained in the small-slip areas at the northern and southern edges of each fault plane (Figs. 3a, c). In both models, the T-axis azimuth, extracted from the resultant potency-density tensors, gradually rotate in the clockwise direction from the hypocentre toward the northern end of the major rupture area (Figs. 3b, d). T-axis azimuths in the small-slip area are inconsistent with those seen in the large-slip area, possibly because of contamination by later phases and the relatively small slip amplitudes at the northern and southern edges of the fault plane. The inverted total seismic moment was 1.965×10^{21} Nm (M_W 8.1) for the N1 fault plane and 1.931×10^{21} Nm (M_W 8.1) for the N2 fault plane; these values are slightly larger than both the USGS W-phase solution of 1.14×10^{21} Nm (M_W 8.0) and the GCMT solution of 1.23×10^{21} Nm (M_W 8.0). The waveform fittings between observed and synthetic waveforms show good agreement, with variance reductions of 72.3% for the N1 model and 70% for the N2 model.

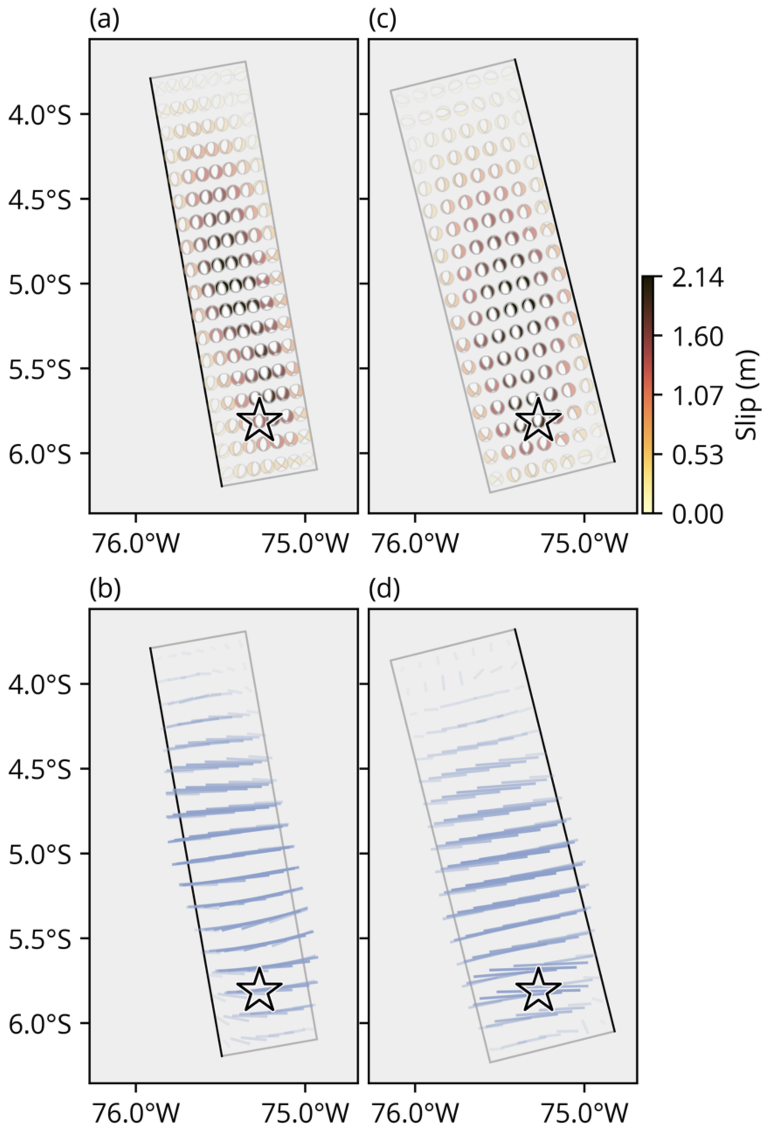

Figure 3: Static slip distribution of the N1 and N2 models. (a) The beachballs show the moment-tensor solutions from the N1 model. The colour represents the slip. (b) The T-axis azimuth distribution for the N1 model, whose length is scaled with the slip. The star shows the epicentre. The rectangle outlines the model plane geometry. The black line is a top of the model plane. (c) and (d) are the same as (a) and (b) but for the N2 model.

Figure 4 shows snapshots of the N1 and N2 models. In both models, the rupture propagates downdip from the hypocentre for 15 s after the initial break. In the N1 model, the initial rupture propagates eastward, whereas it propagates westward in the N2 model.

From 15 to 30 s after the initial break, the rupture propagates unilaterally northward in both models. Then at 30 s, the rupture begins to propagate bilaterally toward both the north and south, and a large slip occurs on the downdip side of the hypocentre near where the initial rupture occurred in both models. Then, 45 s after the initial break, the rupture propagates unilaterally northward again. The rupture finally stops about 200 km north of the epicentre. A synthetic test performed to evaluate the robustness of the waveform inversion result showed that these rupture behaviours are well reproduced (see Text S1).

We also performed the BP with the fault planes N1 and N2 by computing the travel times between the possible sources and the stations (Figs. 5a and S4a). In both the models using the high-frequency (0.3–2.0 Hz) waveforms, the relatively intense BP signals appear east of the epicenter during the initial rupture process (within ~15 s of the initial break). From 20 to 30 s, another intense BP signals can be seen around 20 to 80 km north of the epicenter. At ~40 s, we observed the intense BP signals at 20 km south of the epicenter, then, at ~50 s, another intense BP signals can be seen at 100 km north of the epicenter. We also observe several modest patches of the BP signals in the later time, and it ceased at ~60 s. The low-frequency (0.1–0.5 Hz) BP result (Figs. 5b and S4b) shares the similar spatiotemporal signal distributions with those in the high-frequency BP results; the dominant northern signal migration and the peculiar appearance of the intense BP signals at the southern part of the model space at ~40 s from the hypocentral time, but they show relatively smoother signal distributions than the high-frequency BP results (Figs. 5 and S4).

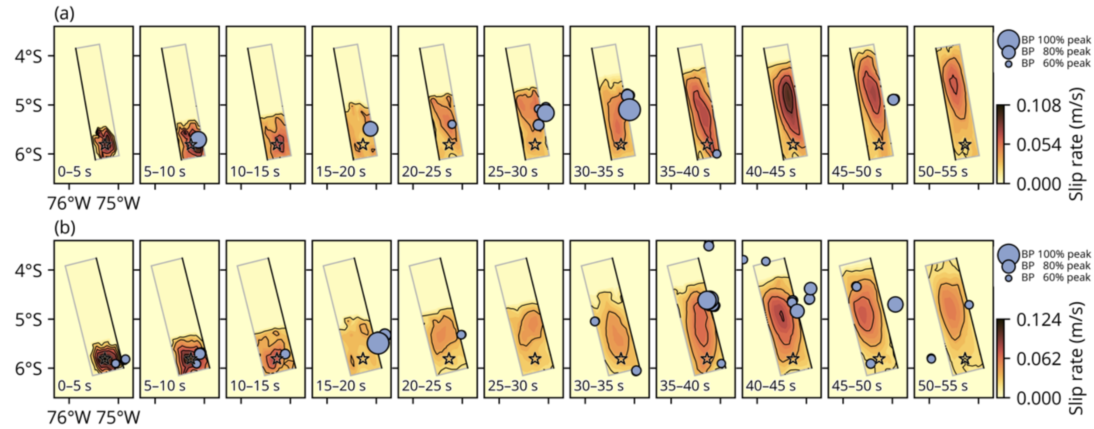

Figure 4: Snapshots of slip-rate distribution and the BP signals for the N1 and N2 fault planes. The circles indicate the relatively intense BP signals larger than 60% of the maximum peak. The time window of each snapshot is on left-bottom. The black star indicates the epicentre, and the black contour interval of slip-rate is 0.02 m/s. The rectangle outlines the model plane geometry. The black line is a top of the model plane.

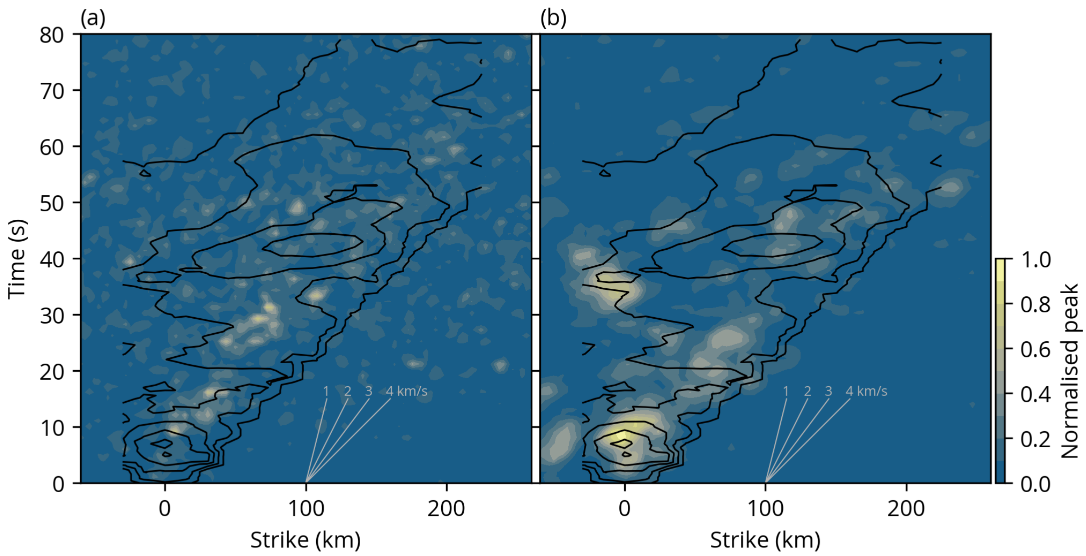

Figure 5: Finite-fault inversion and BP results for the N1 fault plane. The background colour shows the normalized peak of the BP results by using the (a) 0.3–2.0 Hz and (b) 0.1–0.5 Hz bandpass filtered waveforms. The contour interval of the slip-rate is 0.02 m/s. The grey lines show the reference rupture speeds.

4. Discussion

4.1. Evaluation of the primary fault plane of the 2019 Peru earthquake

In ordinary finite-fault inversion, the selection of the primary fault plane from the two possible nodal planes obtained from the moment tensor solution is usually based on the aftershock distribution or the surface rupture geometry; then, the slip-rate distribution is estimated for the selected fault plane (e.g., Legrand and Delouis, 1999). However, for an intermediate-depth earthquake associated with low aftershock activity such as the 2019 Peru earthquake, it is difficult to uniquely identify the primary fault plane. It might be possible to select the primary fault plane if the main rupture propagation direction can be determined by examining the pulse width of the observed waveforms (e.g., Legrand and Delouis, 1999). However, even if a seismic source model in which both planes satisfy the major rupture direction can be constructed, selecting the primary fault plane is still difficult because for both fault planes the waveform variances between synthetic and observed waveforms would have nearly identical values (e.g., Julian et al., 1998; Ye et al., 2020). Even though the variance of the waveform fittings differed by 2.3% between our N1 and N2 models indicating that the N1 nodal plane is the causative fault plane, the spatial distribution of the slip and focal mechanisms and the snapshots in both the two assumed fault planes are interpretable and reasonable. The determination of the primary fault plane of the 2019 Peru earthquake by only finite-fault inversion is in doubt, we therefore proposed the way combining with the finite-fault inversion and BP to further evaluate the likeliness of the primary fault plane of the 2019 Peru earthquake.

In general, the Green's function of teleseismic body waves describes not only the direct *P* phase but also phases reflected from the ground surface in the near-source region (i.e., the *pP* and *sP* phases), which contain useful information on the depth of the radiation source. In finite-fault inversion, a high resolution in the depth direction can be obtained that can explain waveforms overall, including the reflected phases (e.g., Yagi et al., 2004). In our study, snapshots of the slip distribution on the N1 and N2 fault planes show spatial differences in rupture propagation (Fig. 4). During the initial rupture, the finite-fault inversion for the N1 model resolved an eastward downdip rupture, whereas the N2 model showed downdip westward propagation. Thus, in both the N1 and N2 models, the finite-fault inversion had good resolution in the depth direction, as shown by the downdip propagation of the initial rupture in both models, but not in the horizontal rupture direction. In contrast, the BP results showed that the initial rupture propagated eastward on both the fault planes (Fig. 4). Similarly, in the finite-fault inversion result for the main rupture on the southern part of the fault plane, the inverted slip near the hypocenter from 35 to 45 s is on the east and west side of the hypocenter in the N1 and N2 model, respectively. In contrast, the BP results showed that *P*-waves with strong intensity radiated eastward from the epicenter on both the fault planes. Given the consistency of the rupture direction on the N1 fault plane between the inversion and BP imaging results, the rupture paths are located to the east of the epicenter. We therefore selected the eastward-dipping N1 fault plane as likely the preferred fault plane for the 2019 Peru earthquake.

4.2. Detailed rupture process with a back-propagating rupture

The initial rupture begins around the hypocentre at 0 to 5 s and then propagates downdip from the hypocentre at a high slip rate. From 15 s, the rupture propagates northward from the epicentre, and a high slip rate is observed north of the epicentre during 15 to 30 s (Fig. 4a). The intense BP signals appear to the east of the epicentre and move north of the epicentre during the first ~15 s. It is known that intense high-frequency waves can be radiated as a result of a rapid change of rupture-front velocity, slip velocity, or both (e.g., Madariaga, 1977; Spudich and Frazer, 1984; Yagi and Okuwaki, 2015). The multiple energy burst spots located around the rupture front correspond to fluctuations in the rupture propagation rate. The patchy BP image may also reflect artifact sources related to the high-frequency reflection/refraction waves. In our BP analysis, however, we use the globally observed stations with the good azimuthal coverage, which could generally enhance the spatial resolution and suppress the known swimming artifacts, originated from using the narrow aperture array stations (Fukahata et al., 2014; Okuwaki et al., 2015). The first peak of the moment rate function (Fig. S1b) also suggests that the first rupture episode with small seismic energy occurs during 0 to 15 s. We therefore inferred that, following the initial rupture propagation downdip from the hypocentre, the rupture propagated unilaterally northward from the epicentre.

From 15 to 45 s, a high-slip-rate area appears to the north of the epicenter (15 to 30 s) that then expands bilaterally, both northward and southward, from 30 to 45 s (Fig. 5). During this rupture stage, we observe the strong BP signals during 15 to 30 s at ~60 km north of the epicentre, just before the rupture begins to propagate bilaterally both northward and southward from the epicenter, which suggests the BP signals during 15 to 30 s is interpreted as bilateral rupture acceleration, including back-rupture propagation toward the south. During the southward back-rupture propagation, the strong BP signal is observed at ~40 s, around 25 km south of the epicenter (Fig. 6). Because this BP signal is at the southern edge of the rupture zone, where the slip rate decreases, it likely corresponds to the deceleration or termination of the southward back-propagating rupture. Notably, the IRIS-DMC automated BP product also shows weak BP signals at 30 to 40 s near the epicentre (http://ds.iris.edu/spud/backprojection/17616500, last accessed on 2021-06-15). Furthermore, Vallée et al. (2020), using the Multitaper-MUSIC BP method (Meng et al., 2011) independently found similar high-frequency signal emissions back-propagating from north to south of the epicentre. If the BP signals during 15 to 30 s and ~40 s are the signature of continuous back-propagation from north to south of the epicentre, then the rupture-front velocity can be estimated as approximately at 4 km/s (0.85 V_S) (V_s is the shear wave velocity) along the strike of the fault plane (Fig. 6). Our observation of the back-rupture propagation is similar to what is proposed in the numerical simulations (Gabriel et al., 2012; Idini & Ampuero, 2020) and the recent finding during the M_W 7.1 2016 Romanche transform-fault earthquake (Hicks et al., 2020). Alternatively, a rupture path with a slow rupture-front velocity of <1 km/s could be drawn directly from the initial BP signals during 0-15 s to the BP signals in south of the epicentre ~40 s (Fig. 6). Although such the slow rupture migration is possible for the deep earthquakes (e.g. Kanamori et al., 1998; Suzuki and Yagi, 2011), the rupturing path from the hypocentre to ~25 km south of the hypocentre (~40 s) is not clearly seen from both the finite-fault model and the low-frequency and high-frequency BP results (Figs. 5 and 6), compared to the one from the hypocentre to ~60 km north from the hypocentre until ~30 s (Figs. 5 and 6). It is also possible that in a narrow model space, such an apparent, sudden stop of the southern rupture behaviour might be artificially observed by finite-fault inversion. We tested this hypothesis by adopting a longer model space, with 60 km model plane length south of the epicentre, and we confirmed that, consistent with the rupture behaviour in the shorter model space, the southward rupture robustly stopped at ~30 km south of the epicentre (Fig. S7).

Following the north-south bilateral rupture, the rupture pattern returns to northern unilateral propagation. At ~50 s, we observe the BP signals at ~100 km north of the epicentre (Fig. 6). The high-slip rate associated with the BP signals at 100 km north of the epicentre can therefore correspond to northward rupture acceleration. Then, the rupture propagation finally halts in the area ~200 km north of the epicentre (Fig. 6).

Thus, the BP signals at ~60 s can correspond to rupture deceleration at the northern edge of the fault plane, indicating termination of the rupture.

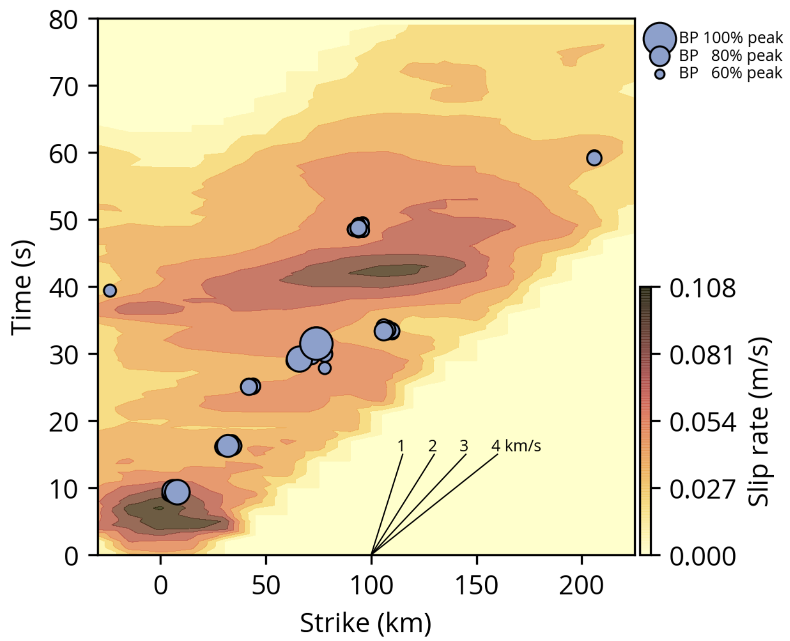

Figure 6: Time evolution of slip rate and the BP along the strike direction for the N1 fault plane. The lines show the reference rupture speeds.

The distribution of T-axis azimuths, extracted from the resultant potency-density tensors, shows gradual clockwise rotation from the epicentre northward, and the large-slip area from 50 to 150 km north of the hypocentre corresponds to the high curvature area of the slab iso-depth lines (Fig. 7). The synthetic test showed that the T-axis azimuth rotation was well restored in the output model (Fig. S3b). The rotation of the T-axis azimuths is well correlated with that of the slab strike. In general, accumulation of extensional stress associated with slab bending is one cause of intraslab earthquakes (e.g., Astiz et al., 1988; Okuwaki and Yagi, 2017). The apparent consistency between the T-axis azimuths and the slab geometry suggests that the 2019 Peru earthquake was caused by extensional stress generated by the slab bending and that the rupture process of the 2019 Peru earthquake was controlled by the slab geometry. While Ranero et al. (2005) found that, in Middle America and Chile subduction zones, the patterns of nodal-planes orientation of intermediate-depth earthquakes in slab is similar to those of the near-trench bending-related earthquakes, which is not consistent with the slab geometry, suggesting that the intermediate-seismicity is a result of reactivation of faults formed by the plate bending near the trench. Given the possible uncertainty of slab-geometry model and the limited seismicity in the source region of the 2019 Peru earthquake, however, it is difficult to uniquely eliminate either the possibility of fault reactivation or the slab bending for the occurrence of the 2019 Peru earthquake alone, and a future study, together with a high-resolution bathymetry map of the sea-floor fabric, will evaluate whether this rotation of the T-axis azimuth along ~200-km-long fault is a result of fault reactivation. We also note that it is possible that the T-axis rotation observed in this study does not necessarily represent the curved geometry of the one sole fault, but also indicates the distinct multiple faults either aligned along the orientation of the slab, or independently aligned by the other structures in the slab, e.g., the inherited ocean fabrics developed before the subduction, though these possibilities are currently difficult to discriminate primarily because of the limited spatial resolution of our teleseismic finite-fault inversion.

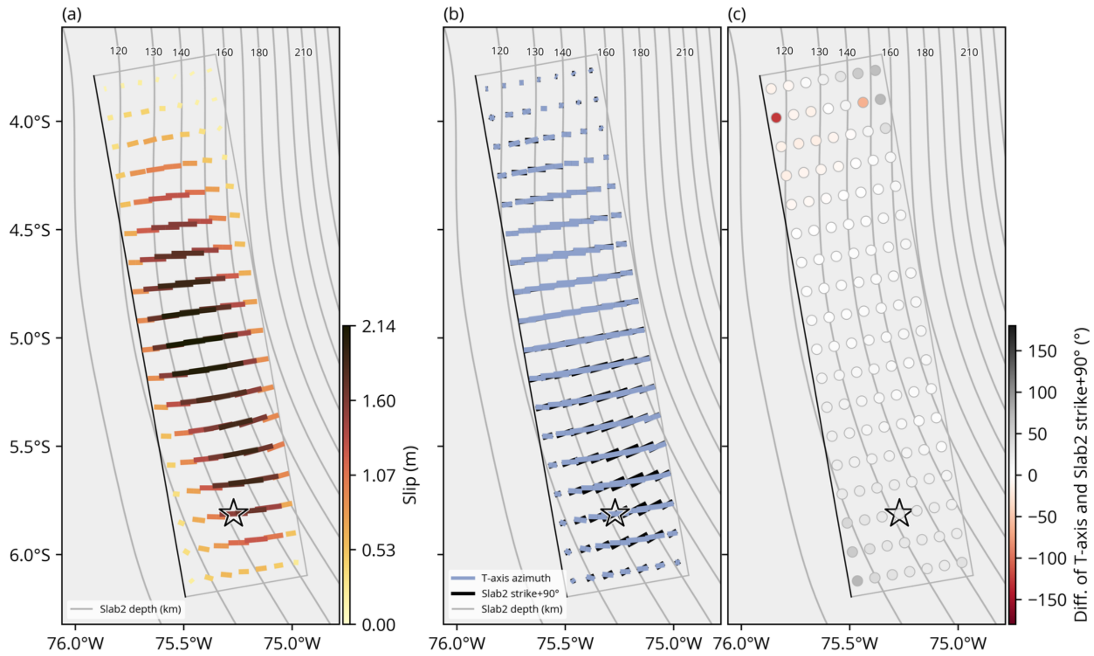

Figure 7: (a) Spatial distribution of T-axis azimuth distribution in the N1 fault plane. (b) The comparison between T-axis azimuth for the N1 fault plane and the Slab2 model (Hayes et al., 2018). The contours are iso-depths (km) of the Slab2 model (Hayes et al., 2018). The The rectangle outlines the model plane geometry. The black line is a top of the model plane.

The inverted source model shows a complex rupture pattern, including back-rupture propagation and the rotation of T-axis azimuth, but the total slip distribution in the inverted model was smoother than in previous studies (e.g., Liu and Yao, 2020; Ye et al., 2020). This difference in smoothing may be explained by the fact that we used a seismic source model with high degrees of freedom and determined the optimal values of the hyperparameters, including smoothing strength, by minimizing Akaike's Bayesian Information Criterion (Akaike, 1980; Yabuki and Matsu'ura, 1992; Yagi and

Fukahata, 2011). It is worth noting that the smooth source model well explains the characteristics of the observed velocity waveforms, including the high-frequency components (Fig. S2).

4.3. Scaling relationships and the abnormal source characteristics of the 2019 Peru earthquake

The physical nature of the intermediate-depth intraslab earthquake, especially the ones occurring at deeper than 100 km, is generally difficult to investigate, primarily because of the lack of aftershock (e.g., Persh and Houston 2004a). Yet, by analysing the complex broadband waveforms, the source characteristics of the deep intermediate-depth intraslab earthquakes have been investigated. The scaling relationship between the source duration τ and the seismic moment M_0 is found to follow $\tau \propto M_0^{0.25\sim0.26}$ (Persh and Houston, 2004b; Poli and Prieto, 2014). Whilst our preferred finite-fault model for the N1 fault plane shows the source duration at 80 s and the seismic moment of 1.965×10^{21} Nm, which is over two times longer than the expected duration (~35 s) from the scaling relationship (Persh and Houston, 2004b). The stress drop of the deep and intermediate-depth earthquakes is generally larger than the shallow crustal earthquakes. For example, Poli and Prieto (2016) found the median stress drop 14.8 MPa through the measurements of the source duration and the radiated seismic energy, which reflects the variety of large frictional stresses for the deep and intermediate-depth earthquake. We estimated the stress drop $\Delta\sigma_0$ for the 2019 Peru earthquake by the relationship with the seismic moment M_0 and the fault area S of $\Delta\sigma_0 = 2.5M_0/S^{1.5}$ (Kikuchi and Fukao, 1980). By assuming an effective fault area as 200 x 90 km^2 and the seismic moment 1.965×10^{21} Nm of our preferred N1 model, the stress drop estimates 2.03 MPa, which is comparable to the estimates by Ye et al. (2020). The estimated stress drop for the 2019 Peru earthquake is significantly lower than the median stress drop for the deep and intermediate-depth earthquakes (Poli and Prieto, 2016). Those abnormal source characteristics of the 2019 Peru earthquake collectively suggests the rupture complexity among the multiple rupture stages involving the back-rupture propagating, which contributes to the longer source duration, and the highly heterogeneous distribution of fault strength/stress that enables the abnormal back-rupture propagation.

5. Conclusion

We applied a newly developed finite-fault teleseismic waveform inversion method and the BP method to estimate the detailed rupture process of the 2019 Peru intraslab earthquake. Integrated use of the finite-fault inversion and BP methods made it feasible to select the primary fault plane of the main shock, because the finite-fault inversion and the BP were consistent in showing eastward rupture propagation only on an east-dipping fault plane during the rupture process. Our study revealed that the 2019 Peru earthquake ruptured a steeply dipping normal fault with multiple rupture episodes. The initial downdip and eastward rupture episode around the hypocentre was followed by a northward rupture episode. Then, the main bilateral rupture episode propagated both northward and southward of the epicentre and was followed by a unilateral northward rupture episode. Most notably, the southern wing of the main bilateral rupture back-propagated through the initial rupture area. The estimated potency-density tensor for each source element in the finite-fault model revealed that the clockwise rotation of T-axis azimuths corresponded well to the change in the strike of the Nazca slab in the large-slip area. These findings suggest that the 2019 Peru earthquake resulted from extensional stress generated by slab bending and the source process was controlled by the slab geometry.

Acknowledgements

We thank the editor Dr Eiichi Fukuyama, the assistant editor Dr Louise Alexander, the reviewer Dr Stephen Hicks, and the anonymous reviewer for evaluating the manuscript. This work was supported by a Grant-in-Aid for Scientific Research (C) 19K04030. The facilities of IRIS Data Services, and specifically the IRIS Data Management Center, were used for access to waveforms, related metadata, and derived products used in this study. IRIS Data Services are funded through the Seismological Facilities for the Advancement of Geoscience (SAGE) Award of the National Science Foundation under Cooperative Support Agreement EAR-1851048. The figures were generated with matplotlib (Hunter, 2007) and Generic Mapping Tools (Wessel et al., 2013). Waveform data were downloaded via the IRIS Wilber 3 system (https://ds.iris.edu/wilber3) from

the following networks: the Canadian National Seismograph Network (CN; https://doi.org/10.7914/SN/CN); the GEOFON Seismic Network (GE; https://doi.org/10.14470/TR560404); the Netherlands Seismic and Acoustic Network (NL; https://doi.org/10.21944/e970fd34-23b9-3411-b366-e4f72877d2c5); the GEOSCOPE (G; https://doi.org/10.18715/GEOSCOPE.G); the IRIS/IDA Seismic Network (II; https://doi.org/10.7914/SN/II); the International Miscellaneous Stations (IM; https://www.fdsn.org/networks/detail/IM/); the Global Seismograph Network (IU; https://doi.org/10.7914/SN/IU), the Global Telemetered Seismograph Network (GT; https://doi.org/10.7914/SN/GT) and the Berkeley Digital Seismograph Network (BK; https://doi.org/10.7932/BDSN).

References

Akaike, H. (1980). Likelihood and the Bayes procedure. *Trab. Estad. Y Investig. Oper.*, *31*(1), 143–166. https://doi.org/10.1007/BF02888350

Astiz, L., Lay, T., & Kanamori, H. (1988). Large intermediate-depth earthquakes and the subduction process. *Phys. Earth Planet. Inter.*, *53*(1–2), 80–166. https://doi.org/10.1016/0031-9201(88)90138-0

DeMets, C., Gordon, R. G., & Argus, D. F. (2010). Geologically current plate motions. *Geophys. J. Int.*, *181*(1), 1–80. https://doi.org/10.1111/j.1365-246X.2009.04491.x

Derode, B., & Campos, J. (2019). Energy Budget of Intermediate-Depth Earthquakes in Northern Chile: Comparison With Shallow Earthquakes and Implications of Rupture Velocity Models Used. *Geophys. Res. Lett.*, *46*(5), 2484–2493. https://doi.org/10.1029/2018GL080962

Di Toro, G., Han, R., Hirose, T., De Paola, N., Nielsen, S., Mizoguchi, K., … Shimamoto, T. (2011). Fault lubrication during earthquakes. *Nature*, *471*(7339), 494–498. https://doi.org/10.1038/nature09838

Duputel, Z., Agram, P. S., Simons, M., Minson, S. E., & Beck, J. L. (2014). Accounting for prediction uncertainty when inferring subsurface fault slip. *Geophys. J. Int.*, *197*(1), 464–482. https://doi.org/10.1093/gji/ggt517

Dziewonski, A. M., Chou, T.-A., & Woodhouse, J. H. (1981). Determination of earthquake source parameters from waveform data for studies of global and regional seismicity. *J. Geophys. Res. Solid Earth*, *86*(B4), 2825–2852. https://doi.org/10.1029/JB086iB04p02825

Ekström, G., Nettles, M., & Dziewoński, A. M. (2012). The global CMT project 2004–2010: Centroid-moment tensors for 13,017 earthquakes. *Phys. Earth Planet. Inter.*, *200–201*, 1–9. https://doi.org/10.1016/j.pepi.2012.04.002

Fukahata, Y., Yagi, Y., & Rivera, L. (2014). Theoretical relationship between back-projection imaging and classical linear inverse solutions. *Geophys. J. Int.*, *196*(1), 552–559. https://doi.org/10.1093/gji/ggt392

Gabriel, A.-A., Ampuero, J.-P., Dalguer, L. A., & Mai, P. M. (2012). The transition of dynamic rupture styles in elastic media under velocity-weakening friction. *J. Geophys. Res. Solid Earth*, *117*(B9), 1–20. https://doi.org/10.1029/2012JB009468

Gutenberg, B., & Richter, C. (1949). Seismicity of the Earth and Associated Phenomena. *Princet. Univ. Press*. Retrieved from https://books.google.co.uk/books?id=YOcKAQAAIAAJ

Hacker, B. R., Peacock, S. M., Abers, G. A., & Holloway, S. D. (2003). Subduction factory 2. Are intermediate-depth earthquakes in subducting slabs linked to metamorphic dehydration reactions? *J. Geophys. Res. Solid Earth*, *108*(B1). https://doi.org/10.1029/2001JB001129

Hartzell, S. H., & Heaton, T. H. (1983). Inversion of strong ground motion and teleseismic waveform data for the fault rupture history of the 1979 Imperial Valley, California, earthquake. *Bull. Seism. Soc. Am.*, *73*(6A), 1553.

Hayes, G. P., Moore, G. L., Portner, D. E., Hearne, M., Flamme, H., Furtney, M., & Smoczyk, G. M. (2018). Slab2, a comprehensive subduction zone geometry model. *Science (80-.).*, *362*(6410), 58–61. https://doi.org/10.1126/science.aat4723

Hicks, S. P., Okuwaki, R., Steinberg, A., Rychert, C. A., Harmon, N., Abercrombie, R. E., … Sudhaus, H. (2020). Back-propagating supershear rupture in the 2016 Mw 7.1 Romanche transform fault earthquake. *Nat. Geosci.*, *13*(9), 647–653. https://doi.org/10.1038/s41561-020-0619-9

Houston, H. (2007). Deep Earthquakes. In G. B. T.-T. on G. Schubert (Ed.), *Treatise on Geophysics* (pp. 321–350). https://doi.org/10.1016/B978-044452748-6.00071-7

Hunter, J. D. (2007). Matplotlib: A 2D Graphics Environment. *Comput. Sci. Eng.*, *9*(3), 90–95. https://doi.org/10.1109/MCSE.2007.55

Ide, S., & Takeo, M. (1996). The dynamic rupture process of the 1993 Kushiro-oki earthquake. *J. Geophys. Res. Solid Earth*, *101*(B3), 5661–5675. https://doi.org/10.1029/95JB00959

Idini, B., & Ampuero, J.-P. (2020). Fault-Zone Damage Promotes Pulse-Like Rupture and Back-Propagating Fronts via Quasi-Static Effects. *Geophys. Res. Lett.*, *47*(23), e2020GL090736. https://doi.org/10.1029/2020GL090736

Ishii, M., Shearer, P. M., Houston, H., & Vidale, J. E. (2005). Extent, duration and speed of the 2004 Sumatra–Andaman earthquake imaged by the Hi-Net array. *Nature*, *435*(7044), 933–936. https://doi.org/10.1038/nature03675

Julian, B. R., Miller, A. D., & Foulger, G. R. (1998). Non-double-couple earthquakes 1. Theory. *Rev. Geophys.*, *36*(4), 525–549. https://doi.org/10.1029/98RG00716

Kaila, K. L., Krishna, V. G., & Khandekar, G. (1999). Preliminary models of upper mantle P and S wave velocity structure in the western South America region. *J. Geodyn.*, *27*(4–5), 567–583. https://doi.org/10.1016/S0264-3707(98)00016-7

Kanamori, H., Anderson, D. L., & Heaton, T. H. (1998). Frictional Melting During the Rupture of the 1994 Bolivian Earthquake. *Science (80-.).*, *279*(5352), 839–842. https://doi.org/10.1126/science.279.5352.839

Kelemen, P. B., & Hirth, G. (2007). A periodic shear-heating mechanism for intermediate-depth earthquakes in the mantle. *Nature*, *446*(7137), 787–790. https://doi.org/10.1038/nature05717

Kennett, B. L. N., Engdahl, E. R., & Buland, R. (1995). Constraints on seismic velocities in the Earth from traveltimes. *Geophys. J. Int.*, *122*(1), 108–124. https://doi.org/10.1111/j.1365-246X.1995.tb03540.x

Kikuchi, M., & Fukao, Y. (1988). Seismic wave energy inferred from long-period body wave inversion. *Bull. Seismol. Soc. Am.*, *78*(5), 1707–1724.

Kikuchi, M., & Kanamori, H. (1991). Inversion of complex body waves-III. *Bull. Seism. Soc. Am.*, *81*(6), 2335–2350.

Kiser, E., & Ishii, M. (2017). Back-Projection Imaging of Earthquakes. *Annu. Rev. Earth Planet. Sci.*, *45*(1), 271–299. https://doi.org/10.1146/annurev-earth-063016-015801

Krüger, F., & Ohrnberger, M. (2005). Tracking the rupture of the Mw = 9.3 Sumatra earthquake over 1,150 km at teleseismic distance. *Nature*, *435*(7044), 937–939. https://doi.org/10.1038/nature03696

Legrand, D., & Delouis, B. (1999). Determination of the fault plane using a single near-field seismic station with a finite-dimension source model. *Geophys. J. Int.*, *138*(3), 801–808. https://doi.org/10.1046/j.1365-246x.1999.00917.x

Liu, W., & Yao, H. (2020). Rupture Process of the 26 May 2019 M w 8.0 Northern Peru Intermediate-Depth Earthquake and Insights Into Its Mechanism. *Geophys. Res. Lett.*, *47*(4), e2020GL087167. https://doi.org/10.1029/2020GL087167

Ma, Y., & Clayton, R. W. (2014). The crust and uppermost mantle structure of Southern Peru from ambient noise and earthquake surface wave analysis. *Earth Planet. Sci. Lett.*, *395*, 61–70. https://doi.org/10.1016/j.epsl.2014.03.013

Madariaga, R. (1977). High-frequency radiation from crack (stress drop) models of earthquake faulting. *Geophys. J. Int.*, *51*(3), 625–651. https://doi.org/10.1111/j.1365-246X.1977.tb04211.x

McCloskey, J., Lange, D., Tilmann, F., Nalbant, S. S., Bell, A. F., Natawidjaja, D. H., & Rietbrock, A. (2010). The September 2009 Padang earthquake. *Nat. Geosci.*, *3*(2), 70–71. https://doi.org/10.1038/ngeo753

Melgar, D., Pérez-Campos, X., Ramirez-Guzman, L., Spica, Z., Espíndola, V. H., Hammond, W. C., & Cabral-Cano, E. (2018). Bend Faulting at the Edge of a Flat Slab: The 2017 M w 7.1 Puebla-Morelos, Mexico Earthquake. *Geophys. Res. Lett.*, *45*(6), 2633–2641. https://doi.org/10.1002/2017GL076895

Meng, L., Inbal, A., & Ampuero, J.-P. (2011). A window into the complexity of the dynamic rupture of the 2011 Mw 9 Tohoku-Oki earthquake. *Geophys. Res. Lett.*, *38*(7), n/a-n/a. https://doi.org/10.1029/2011GL048118

Muirhead, K. J., & Datt, R. (1976). The N-th root process applied to seismic array data. *Geophys. J. Int.*, *47*(1), 197–210. https://doi.org/10.1111/j.1365-246X.1976.tb01269.x

Okuwaki, R., & Yagi, Y. (2017). Rupture Process During the M w 8.1 2017 Chiapas Mexico Earthquake: Shallow Intraplate Normal Faulting by Slab Bending. *Geophys. Res. Lett.*, *44*(23), 11,816-11,823. https://doi.org/10.1002/2017GL075956

Okuwaki, R., Yagi, Y., & Hirano, S. (2015). Relationship between High-frequency Radiation and Asperity Ruptures, Revealed by Hybrid Back-projection with a Non-planar Fault Model. *Sci. Rep.*, *4*(1), 7120. https://doi.org/10.1038/srep07120

Olson, A. H., & Apsel, R. J. (1982). Finite faults and inverse theory with applications to the 1979 Imperial Valley earthquake. *Bull. Seism. Soc. Am.*, *72*(6A), 1969.

Perfettini, H., Avouac, J.-P., Tavera, H., Kositsky, A., Nocquet, J.-M., Bondoux, F., … Soler, P. (2010). Seismic and aseismic slip on the Central Peru megathrust. *Nature*, *465*(7294), 78–81. https://doi.org/10.1038/nature09062

Persh, S. E., & Houston, H. (2004). Strongly Depth-Dependent Aftershock Production in Deep Earthquakes. *Bull. Seismol. Soc. Am.*, *94*(5), 1808–1816. https://doi.org/10.1785/012003191

Persh, S. E., & Houston, H. (2004). Deep earthquake rupture histories determined by global stacking of broadband P waveforms. *J. Geophys. Res. Solid Earth*, *109*(B4). https://doi.org/10.1029/2003JB002762

Poli, P., & Prieto, G. (2014). Global and along-strike variations of source duration and scaling for intermediate-depth and deep-focus earthquakes. *Geophys. Res. Lett.*, *41*(23), 8315–8324. https://doi.org/10.1002/2014GL061916

Poli, P., & Prieto, G. A. (2016). Global rupture parameters for deep and intermediate-depth earthquakes. *J. Geophys. Res. Solid Earth*, *121*(12), 8871–8887. https://doi.org/10.1002/2016JB013521

Prezzi, C. B., & Silbergleit, V. (2015). Seismic hazards along Ecuador, Perú and northern Chile (South America). *Nat. Hazards*, *79*(2), 1159–1175. https://doi.org/10.1007/s11069-015-1900-x

Prieto, G. A., Florez, M., Barrett, S. A., Beroza, G. C., Pedraza, P., Blanco, J. F., & Poveda, E. (2013). Seismic evidence for thermal runaway during intermediate-depth earthquake rupture. *Geophys. Res. Lett.*, *40*(23), 6064–6068. https://doi.org/10.1002/2013GL058109

Ragon, T., Sladen, A., & Simons, M. (2018). Accounting for uncertain fault geometry in earthquake source inversions – I: theory and simplified application. *Geophys. J. Int.*, *214*(2), 1174–1190. https://doi.org/10.1093/gji/ggy187

Ranero, C. R., Villaseñor, A., Phipps Morgan, J., & Weinrebe, W. (2005). Relationship between bend-faulting at trenches and intermediate-depth seismicity. *Geochemistry, Geophys. Geosystems*, *6*(12), n/a-n/a. https://doi.org/10.1029/2005GC000997

Renshaw, C. E., & Schulson, E. M. (2013). Are intermediate depth earthquakes caused by plastic faulting? *Earth Planet. Sci. Lett.*, *382*, 32–37. https://doi.org/10.1016/j.epsl.2013.09.006

Shimizu, K., Yagi, Y., Okuwaki, R., & Fukahata, Y. (2020). Development of an inversion method to extract information on fault geometry from teleseismic data. *Geophys. J. Int.*, *220*(2), 1055–1065. https://doi.org/10.1093/gji/ggz496

Sladen, A., Tavera, H., Simons, M., Avouac, J. P., Konca, A. O., Perfettini, H., … Cavagnoud, R. (2010). Source model of the 2007 M w 8.0 Pisco, Peru earthquake: Implications for seismogenic behavior of subduction megathrusts. *J. Geophys. Res.*, *115*(B2), B02405. https://doi.org/10.1029/2009JB006429

Somoza, R., & de Hurtis, M. E. (2005). Convergencia en el margen occidental de América del sur durante el Cenozoico: Subducción de Nazca, Farallon y Aluk. *Asoc. Geológica Argentina*.

Spudich, P., & Frazer, L. N. (1984). Use of ray theory to calculate high-frequency radiation from earthquake sources having spatially variable rupture velocity and stress drop. *Bull. Seismol. Soc. Am.*, *74*(6), 2061–2082.

Suzuki, M., & Yagi, Y. (2011). Depth dependence of rupture velocity in deep earthquakes. *Geophys. Res. Lett.*, *38*(5), n/a-n/a. https://doi.org/10.1029/2011GL046807

Tocheport, A., Rivera, L., & Chevrot, S. (2007). A systematic study of source time functions and moment tensors of intermediate and deep earthquakes. *J. Geophys. Res.*, *112*(B7), B07311. https://doi.org/10.1029/2006JB004534

Twardzik, C., & Ji, C. (2015). The Mw7.9 2014 intraplate intermediate-depth Rat Islands earthquake and its relation to regional tectonics. *Earth Planet. Sci. Lett.*, *431*, 26–35. https://doi.org/10.1016/j.epsl.2015.08.033

Uchide, T., Yao, H., & Shearer, P. M. (2013). Spatio-temporal distribution of fault slip and high-frequency radiation of the 2010 El Mayor-Cucapah, Mexico earthquake. *J. Geophys. Res. Solid Earth*, *118*(4), 1546–1555. https://doi.org/10.1002/jgrb.50144

Vallée, M., Grandin, R., Nocquet, J.-M., Villegas, J.-C., Vaca, S., Xie, Y., … Jarrin, P. (2020). Rupture characteristics of the 2019 North Peru intraslab earthquake (Mw8. 0). *EGU General Assembly Conference Abstracts*, 10429. https://doi.org/10.5194/egusphere-egu2020-10429

Villegas-Lanza, J. C., Chlieh, M., Cavalié, O., Tavera, H., Baby, P., Chire-Chira, J., & Nocquet, J.-M. (2016). Active tectonics of Peru: Heterogeneous interseismic coupling along the Nazca megathrust, rigid motion of the Peruvian Sliver, and Subandean shortening accommodation. *J. Geophys. Res. Solid Earth*, *121*(10), 7371–7394. https://doi.org/10.1002/2016JB013080

Wessel, P., Smith, W. H. F., Scharroo, R., Luis, J., & Wobbe, F. (2013). Generic Mapping Tools: Improved Version Released. *Eos, Trans. Am. Geophys. Union*, *94*(45), 409–410. https://doi.org/10.1002/2013EO450001

Wong, I., Dober, M., Hemphill-Haley, M., & Terra, F. (2012). Seismic hazard along the southern coast of Ecuador. *Proceedings of the Fifthteenth World Conference on Earthquake Engineering, Lisbon*, *10*.

Yabuki, T., & Matsu'ura, M. (1992). Geodetic data inversion using a Bayesian information criterion for spatial distribution of fault slip. *Geophys. J. Int.*, *109*(2), 363–375. https://doi.org/10.1111/j.1365-246X.1992.tb00102.x

Yagi, Y., & Fukahata, Y. (2011). Introduction of uncertainty of Green's function into waveform inversion for seismic source processes. *Geophys. J. Int.*, *186*(2), 711–720. https://doi.org/10.1111/j.1365-246X.2011.05043.x

Yagi, Y., Mikumo, T., Pacheco, J., & Reyes, G. (2004). Source Rupture Process of the Tecomán, Colima, Mexico Earthquake of 22 January 2003, Determined by Joint Inversion of Teleseismic Body-Wave and Near-Source Data. *Bull. Seismol. Soc. Am.*, *94*(5), 1795–1807. https://doi.org/10.1785/012003095

Yagi, Y., Nakao, A., & Kasahara, A. (2012). Smooth and rapid slip near the Japan Trench during the 2011 Tohoku-oki earthquake revealed by a hybrid back-projection method. *Earth Planet. Sci. Lett.*, *355–356*, 94–101. https://doi.org/10.1016/j.epsl.2012.08.018

Yagi, Y., & Okuwaki, R. (2015). Integrated seismic source model of the 2015 Gorkha, Nepal, earthquake. *Geophys. Res. Lett.*, *42*(15), 6229–6235. https://doi.org/10.1002/2015GL064995

Ye, L., Lay, T., Bai, Y., Cheung, K. F., & Kanamori, H. (2017). The 2017 M w 8.2 Chiapas, Mexico, Earthquake: Energetic Slab Detachment. *Geophys. Res. Lett.*, *44*(23), 11,824-11,832. https://doi.org/10.1002/2017GL076085

Ye, L., Lay, T., & Kanamori, H. (2020). Anomalously low aftershock productivity of the 2019 M 8.0 energetic intermediate-depth faulting beneath Peru. *Earth Planet. Sci. Lett.*, *549*, 116528. https://doi.org/10.1016/j.epsl.2020.116528